

Evolution of Hen 3-1357, the Stingray Nebula[★]

Miriam Peña¹ †, Mudumba Parthasarathy^{2,3}, Francisco Ruiz-Escobedo¹, and Rajeev Manick⁴

¹*Instituto de Astronomía, Universidad Nacional Autónoma de México, Apdo. Postal 70254, Cd. de México, México*

²*Indian Institute of Astrophysics, Bangalore 560034, India*

³*Department of Physics and Astronomy, Vanderbilt University, 6301 Stevenson Center Ln., Nashville, TN 37235, USA*

⁴*Univ. Grenoble Alpes, CNRS, IPAG, 38000 Grenoble, France*

Accepted 2022 June 21. Received 2022 June 20; in original form 2022 February 22

ABSTRACT

The spectroscopic evolution of Hen 3-1357, the Stingray Nebula, is presented by analysing data from 1990 to 2021. High resolution data obtained in 2021 with South African Large Telescope High Resolution Spectrograph and in 2009 with European Southern Observatory-Very Large Telescope UVES spectrograph are used to determine physical conditions and chemical abundances in the nebula. From comparison of these data with data from different epochs it is found that the intensity of highly-ionized emission lines has been decreasing with time, while the emission of low-ionization lines has been increasing, confirming that the nebula is recombining, lowering its excitation class, as a consequence of the changes in the central star which in 2002 had an effective temperature of 60,000 K and from then it has been getting colder. The present effective temperature of the central star is about 40,000 K. It has been suggested that the central star has suffered a late thermal pulse and it is returning to the AGB phase. The nebular chemistry of Hen 3-1357 indicates that all the elements, except He and Ne, present sub solar abundances. The comparison of the nebular abundances with the values predicted by stellar nucleosynthesis models at the end of the AGB phase, shows that the central star had an initial mass lower than 1.5 M_⊙. We estimated the ADF(O⁺²) to be between 2.6 and 3.5.

Key words: planetary nebulae: individual: Hen 3-1357 – stars: AGB and post-AGB – stars: evolution

1 INTRODUCTION

The Stingray Nebula (also known as PN G331.3-12.1 and Hen 3-1357) is a very young and compact planetary nebula (PN), around the rapidly evolving hot post-Asymptotic Giant Branch (post-AGB) central star SAO 244567, whose post-AGB character was pointed out by Parthasarathy & Pottasch (1989). The compact fully-ionized nebula was discovered by Parthasarathy et al. (1993) and, together with the central star, they have been the subject of multiple studies due to they show unexpected variations. In particular the star, classified as a B-type star in the early 1980s, has been fading by about 1 mag per decade (Schaefer & Edwards 2015), and also its effective temperature has shown rapid changes with time.

A relatively detailed description of the previous studies is presented in this introduction, as it is important for our analysis.

Hubble Space Telescope (HST) high resolution images of Hen 3-1357 showed the presence of a 1.67×0.92 arcsec² nebula around the central star. The HST images also revealed the presence of collimated outflows (Bobrowsky et al. 1998).

A deep review of the stellar and nebular evolution can be found in Balick et al. (2021). In this article the authors analysed the evolution of the nebular shape and the large decreases in the nebular emission-line fluxes based on well calibrated images obtained with HST in 1996 and 2016. They concluded that Hen 3-1357 is now a recombination nebula. Earlier, Harvey-Smith et al. (2018), Arkipova et al. (2013),

and Otsuka et al. (2017) also found evidence that the Stingray Nebula is undergoing recombination.

The central star has shown fast spectral evolution. It has evolved from a B1 type post-AGB supergiant into a PN central star in the extremely short timescale of 20 years (Parthasarathy et al. 1993, 1995; Bobrowsky et al. 1998). UV spectra of the object obtained with the International Ultraviolet Explorer (IUE) showed the rapid evolution of the star from 1988 to 1996. P-Cygni profiles of N v (1240 Å) and C iv (1550 Å) lines in the spectra taken in 1988 indicated a terminal wind velocity of 3,500 km s⁻¹. According to Feibelman (1995) and Parthasarathy et al. (1995) this wind seems to have completely ceased by 1994. Also these authors reported that the object faded by a factor of 3 in the UV, from 1988 to 1996. The fading suggested a rapid increase in the effective temperature, T_{eff} , and gravity, g , of the central star that could be rapidly evolving into a DA white dwarf (Parthasarathy et al. 1995). The luminosity, the core mass, the observed rapid evolution and fading of SAO 244567 are not in agreement with the evolution timescales of low or high mass post-AGB stellar models (Miller-Bertolami 2016).

The rapid evolution of the stellar spectral type and effective temperature has been confirmed. In 1950 the spectrum of SAO 244567 was that of a B or A star with weak H α emission (Henize 1976). In 1971 the spectrum was that of a B1-2 supergiant star with a T_{eff} of 21,000 K and in June 1990 the spectrum was that of a planetary nebula (Parthasarathy et al. 1993, 1995). From a photoionization model of the June 1990 nebular spectrum Köpen and Parthasarathy (1996,

† E-mail: miriam@astro.unam.mx

private comm.) derived a T_{eff} of 50,000 K. Thus in a matter of less than 20 years the T_{eff} increased from 21,000 K to 50,000 K.

Reindl et al. (2014) studied all the UV spectra of this object obtained with the IUE, since 1988 to 2006. These authors found that the central star steadily increased its T_{eff} from 38,000 K to a peak value of 60,000 K in 2002, while its surface gravity increased from $\log(g) = 4.8$ to 6.0 and there was a drop in luminosity. SAO 244567 has cooled down significantly since 2002 and is now expanding. According to Reindl et al. (2014, 2017) and Lawlor (2021) the most reasonable explanation for the stellar variations is a late He-shell flash (late thermal pulse, LTP). The star would be now on its way back to the AGB zone. However, respective models are lacking to match the position of SAO 244567 in the $\log(T_{eff})$ – $\log(g)$ plane. The contradiction between observations and theory makes this star particularly interesting. Its fast evolution gives us the unique opportunity to study stellar evolution in real time.

Harvey-Smith et al. (2018) analysed the full suite of Australia Telescope Compact Array data for Hen 3-1357, taken in the 4–23 GHz range of frequencies between 1991 and 2016. The nebular radio flux density declined during that period showing signs of halting that decline between 2013 and 2016. These authors produced a spatially resolved radio image of the Stingray nebula from data obtained in 2005. A ring structure, which appears to be associated with the ring seen in HST images, was visible. In addition, they found a narrow extension of the radio emission towards the eastern and western edges of the nebula, possibly associated with a jet or outflow. The nebular emission-measure derived by these authors decreased between 1992 and 2011, suggesting that the nebula is undergoing recombination.

Arkhipova et al. (2013) carried out low-resolution spectroscopic studies of the Stingray Nebula. They present two different sets of observations, one obtained in August 1992 with the 1.5-m telescope at La Silla Observatory (European Southern Observatory, ESO-Chile) with a Boller & Chivens spectrograph, and other obtained in June 2011 with the 1.9-m telescope at South African Astronomical Observatory (SAAO) and a long-slit spectrograph. These authors also obtained a high-resolution spectrum that allowed them to measure a heliocentric radial velocity of $11.6 \pm 1.7 \text{ km s}^{-1}$ and an expansion velocity of $8.4 \pm 1.5 \text{ km s}^{-1}$ for Hen 3-1357. Arkhipova et al. (2013) computed the nebular physical parameters and chemical abundances concluding that Hen 3-1357 has sub solar abundances. From the comparison of line intensities of different epochs, they found that the low-excitation lines emission (lines of O^+ , N^+ , and S^+), has increased with time, while the high-excitation lines emission (lines of O^{+2} , Ne^{+2} , and Cl^{+2}) decreased by factor of 2, suggesting a decrease in the excitation class of the nebula (defined as $E.C. = 0.45 (F([O III] 5007) / F(H\beta))$, Dopita & Meatheringham 1990).

Otsuka et al. (2017) performed a detailed analysis of Hen 3-1357 based on high-resolution spectra obtained in 2006, covering from the optical to far-IR wavelengths. These authors calculated the nebular abundances using collisionally excited lines (CELs) and recombination lines (RLs). Their RL C/O abundance ratio would indicate that this PN is O-rich, which is also supported by the detection of the broad $9/18 \mu\text{m}$ bands from amorphous silicate grains. The observed nebular abundances can be explained by stellar AGB nucleosynthesis models with initial masses between 1 and $1.5 M_{\odot}$ and metallicity $Z = 0.008$. Otsuka et al. (2017) reported Ne overabundance which might be due to the enhancement of ^{22}Ne isotope in the He-rich intershell. Using the spectrum of the central star synthesized by a TLUSTY model as the ionization source of the PN, they constructed a self-consistent photoionization model to fit the observed quantities and derive the gas and dust masses, dust-to-gas mass ratio, and core mass of the central star. According to this model about 80% of the

total dust mass is from a warm–cold dust component beyond the ionization front.

Since the Otsuka et al. (2017) study of Hen 3-1357 in 2006 there are no high resolution spectra obtained and analysed to understand the variations in the nebula. In 2021 we obtained high resolution spectra with the South African Large Telescope High Resolution Spectrograph (SALT HRS) under the program ID:2021-1-SCI-007 (PI: Manick). In this paper we perform a detailed analysis of these spectra and we also analyse observations made in the ESO-Chile with the Very Large Telescope VLT-U2 and the UVES spectrograph in 2009.

The analysis of these new data, in conjunction with studies presented by different authors along the years, allows us to discuss the evolution of the Stingray Nebula with time. This will lead to a better understanding of the evolution of the central star whose changes are affecting the nebula.

This paper is organized as follows: In §2 the new observations and data reduction are presented. In §3 we discuss the time evolution of line intensities. In §4 the physical parameters and the ionic abundances of the nebula are determined from the intensities of our observed CELs and RLs, which will allow to determine the Abundance Discrepancy Factors (ADF)¹. Also the time evolution of the physical parameters and ionic abundances is presented in this section. Total nebular abundances derived from our work are presented in §5 and they are compared with abundances from other authors. In §6 the discussion can be found. In §7 our conclusions are presented.

2 OBSERVATIONS AND DATA REDUCTION

As said above, the nebula Hen 3-1357 has been observed and studied in multiple occasions. In this work we analyse spectrophotometric data obtained with ESO VLT UVES and SALT HRS spectrographs, performed in the years 2009 and 2021, respectively.

ESO VLT UVES is a high-resolution optical echelle spectrograph located at the Nasmyth B focus of telescope UT2. The light beam of the telescope is split in two arms (blue and red). The resolving power is about 40,000 when a slit width of 1 arcsec is used. The data analysed here were retrieved from the archives, already wavelength and flux calibrated with the procedures described at ESO Data Release 2020. The slit size for the observations was 1×10 arcsec and the extraction slit of the spectra was 39 pix, equivalent to 2.3 arcsec, which implies that all the nebular emission in the slit was extracted.

SALT HRS is an echelle spectrograph working with two arms simultaneously. The blue one covers from 3826 Å to 5583 Å wavelength range and the red one covers from 5473 Å to 8796 Å range. Slit size used for the nebula was 1.2 arcsec (fiber diameter 350 μm). The spectral resolution R (defined as $\lambda/\delta\lambda$) was about 65,000 at 6,000 Å. Three spectra were obtained in May-June 2021. The observations were made with the slit in parallactic angle to minimize the influence of atmospheric dispersion.

Both observing logs, ESO VLT-U2-UVES and SALT HRS, are presented in Table 1.

SALT data were initially calibrated with the HRS pipeline described by Kniazev (2016) which includes bias subtraction, flat-fielding, extraction, wavelength calibration and merging of different orders. Also heliocentric velocity correction was calculated for each spectrum. Afterwards, data were corrected by atmospheric absorption using SALT absorption law and were flux-calibrated by

¹ The ADF is defined as the ratio between abundances derived from RLs and abundances derived from CELs.

using IRAF² standard routines. The flux standard star BD+02d3375, observed with SALT HRS on 2021 July 18th, was used for flux calibration by adopting the calibrated stellar fluxes obtained from HST-STIS CALSPEC Calibration Database as suggested by Kniazev (2017). By employing this standard star a relative spectral calibration can be obtained. No absolute flux calibration is possible since SALT is a telescope with a variable aperture.

The calibrated SALT HRS spectra were combined in one, to improve the signal-to-noise. The blue and red zones of the combined spectra are shown in Fig. 1. The bottom figure shows the faint recombination lines in the 4640 Å to 4690 Å zone, where the most intense recombination lines of O II are located. The intensity of these lines is thousandths or ten thousandths times lower than H β and it is clear that they are perfectly detected and measurable, therefore this figure shows the high quality of the SALT HRS spectra.

The line intensities in ESO VLT UVES and SALT HRS spectra were measured with the IRAF's *splot* routine, by integrating the flux between two given limits over a continuum estimated by eye. Due to the high spectral resolution most lines appear isolated, no blends are affecting our line measurements. More than a hundred nebular lines were measured in the wavelength range from 3826 Å to 8796 Å. Dereddened fluxes from 3770 Å to 7751 Å are presented in columns 6 and 8 of Table 3.1. Uncertainties of intensities were determined taking into account the SNR of the continuum at each side of the line and the line intensity. The uncertainties are included in parenthesis in each case. In the other columns we present the line intensities given by other authors in different epochs.

The logarithmic reddening correction, $c(H\beta)$, was derived from our data by using Cardelli et al. (1989) reddening law by assuming a ratio of total to selective extinction $R_V = 3.1$ and by using the H Balmer decrement (theoretical $H\gamma/H\beta$ and $H\delta/H\beta$ ratios) given by Storey & Hummer (1995) for a temperature of 10,000 K, adequate to the value derived for Hen 3-1357. In all cases, case B recombination theory and a density of 10^3 cm^{-3} were assumed. Values for $c(H\beta)$ derived in this work, and those presented by other authors, are included in Table 3.1.

3 TIME EVOLUTION OF LINE FLUXES

Dereddened fluxes at each wavelength, for the different observations from 1992 to 2021 are listed in Table 3.1, as they were presented by the different authors (no uncertainties have been included for other authors). Along the time important changes in the line intensities are found in this table. It is evident that the collisionally excited [O III] lines 5007, 4959 and 4363 Å have decreased by a factor larger than 2 from 1992 to 2021. Also [Ne III] 3869 and 3967 Å have decreased by factors of 2.9. Additionally the highly ionized lines of [Ar IV] 4711 and 4740 Å have disappeared and they are not detected in 2021 data. Lines of [Cl III] 5517 and 5538 Å decreased by about 1.8 or more and [S III] 6312 Å has decreased by 22%. In addition, He I recombination lines have also diminished. He I 5876 Å decreased by more than 30%, while He I 3867 Å decreased by a factor of almost 2.

From the above it is concluded that the intensity of highly-excited lines, listed in the paragraph above, have been decreasing systematically. On the contrary, line intensities from low-ionized species have increased. That is the case of [Fe III] 4755 and 4881 Å, [N II]

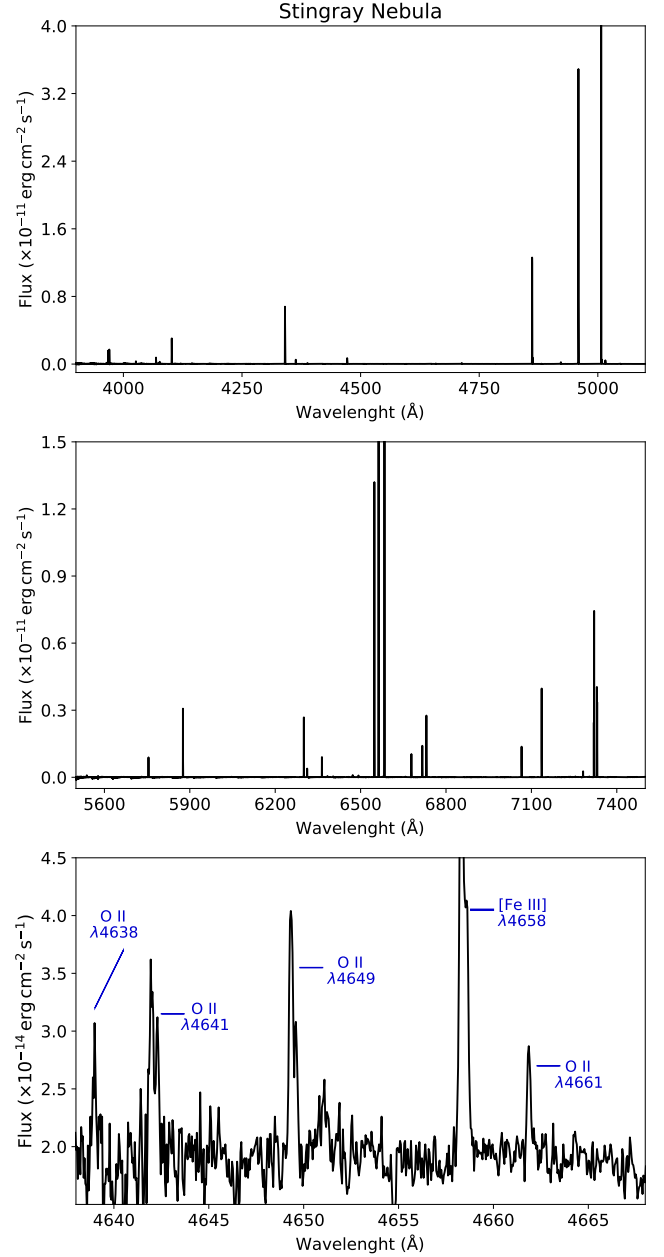


Figure 1. SALT blue and red spectra of Stingray nebula, obtained in 2021. Bottom: SALT spectrum showing the faint recombination lines in the zone 4640 Å to 4670 Å.

6548 and 6583 Å, and [S II] 6716 and 6730 Å whose intensities increased by factors of about 2. Other lines that increased substantially are the [O I] 6300 and 6363 Å lines which in principle do not belong to the ionized nebula and are possibly emitted in an external photo-dissociation zone.

In Fig. 2 the time evolution of some important lines are shown. These line intensity variations are indicating that the nebular excitation class has diminished from about 9 in 1990-1992 to about 4 in 2021. The highly-ionized species are recombining, increasing the ionic abundances of low-ionized species. This evolution is a reaction of the plasma to the fact that the central star is getting colder, probably in its way returning to the AGB zone as a result of a late thermal

² IRAF is distributed by the National Optical Astronomy Observatories, which is operated the Association of Universities for Research in Astronomy, Inc., under contract to the National Science Foundation.

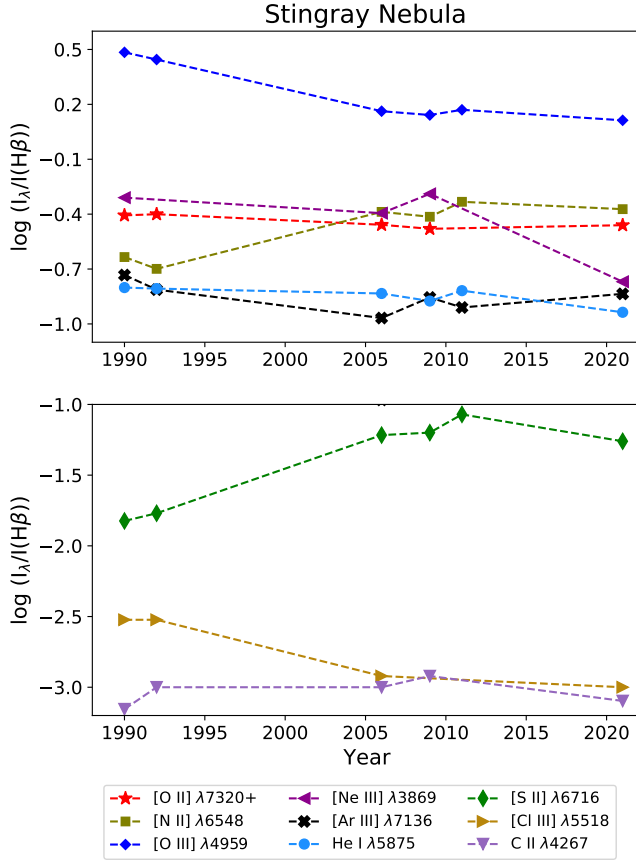


Figure 2. The time evolution of some important lines intensities are plotted. The lines are identified by colours. The upper panel shows the more intense lines.

pulse, LTP, as suggested by Reindl et al. (2014, 2017) and Lawlor (2021).

3.1 RL evolution

He I lines kept the same intensities up to about 2011. In the recent observations with SALT HRS in 2021, these intensities have decreased, most probably due to recombination of He^+ into He^0 . This is confirmed by the fact that He/H total abundance appears lower on 2021, due to only the He^+/H^+ abundance ratio is considered and neutral He is not taken into account (see Table 3).

The C II 4267 Å recombination line, employed to determine C^{+2}/H^+ ionic abundance, and the recombination lines of O II, useful to determine O^{+2}/H^+ ionic abundance, have remained constant.

4 PHYSICAL PARAMETERS OF THE NEBULA

From the nebular lines, in particular from those collisionally excited lines, physical conditions, such as electron densities and temperatures, can be derived from some diagnostic line ratios. In general electron densities can be determined from the [S II] $\lambda\lambda 6731/6716$, [O II] $\lambda\lambda 3729/3726$, [Cl III] $\lambda\lambda 5538/5518$, [Fe III] $\lambda\lambda 4701/4659$, and [Ar IV] $\lambda\lambda 4711/4740$ intensity ratios. Electron temperatures can be obtained from the [N II] $\lambda\lambda (6548+6583)/5755$, [O III] $\lambda\lambda (5007+4959)/4363$,

[Ar III] $\lambda\lambda 7136/5192$, [Ar IV] $\lambda\lambda (7170+7263)/(4711+4740)$, [S II] $\lambda\lambda (6716+6731)/(4068+4076)$ and [O II] $\lambda\lambda 7325/3727$ intensity ratios. The intensity of the auroral line [N II] $\lambda 5755$ was corrected by effects of recombination of N^{+2} using the procedure presented by Liu et al. (2000), by using the ORL abundance of N^{+2} and the temperature determined for CELs, both presented in Table 3; this could be applied only to UVES-2009 data, in which the contribution of recombination to [N II] $\lambda 5755$ line intensity is about 1%.

From the available diagnostic line ratios of the observations presented here, physical conditions were calculated with the code PyNEB (Luridiana et al. 2015), using the atomic data presented in the Appendix B. PyNEB routine *getCrossTemden* was used to determine simultaneously temperatures and densities by building diagnostic diagrams. The uncertainties in the physical conditions and abundances were estimated using Monte Carlo simulations using 400 random points, assuming a normal distribution around each line intensity bounded by the observed flux error.

4.1 Diagnostics diagrams

In Fig. 3 diagnostic diagrams for the ESO VLT-UVES and SALT HRS data analysed here are presented. These diagrams were constructed by using PyNEB, and they show the behaviour of diagnostic line ratios, such as [O III] $\lambda\lambda (4959+5007)/4363$ and [S II] $\lambda\lambda 6731/6716$, as a function of the electron density and temperature.

From the ESO VLT UVES data the available line ratios for temperature determination were those from [N II] $\lambda\lambda (6548+6584)/5755$, and [O III] $\lambda\lambda (4959+5007)/4363$ and the density could be derived from [S II] $\lambda\lambda 6731/6716$, [Ar IV] $\lambda\lambda 4711/4740$ and [Fe III] $\lambda\lambda 4701/4659$. In the case of SALT HRS data, the temperature was determined from [N II], [O III] and [Ar III] diagnostic line ratios, while the density was derived from [S II], [Cl III] and [Fe III] diagnostic line ratios.

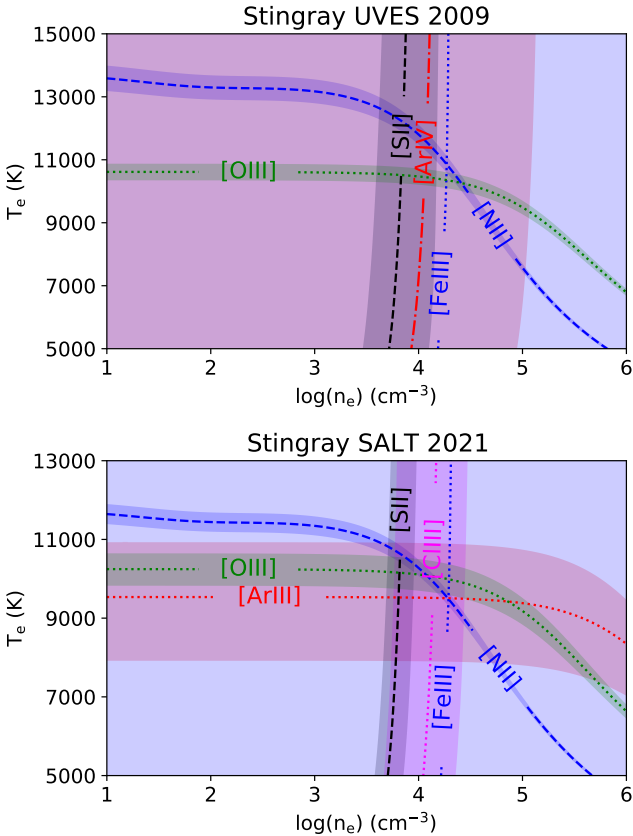
Each line ratio in the diagram is represented by a broken or dotted line inside a colour band which shows the 1σ rms error. The temperature and density values derived from our observations are listed in Table 3. Usually the electron densities and temperatures adopted for ionic abundance determination are obtained from the zone where density- and temperature-diagnostics intersect. In the diagnostic diagrams it is observed that densities from [Ar IV] and [Fe III] are very large and uncertain and will not be used for this purpose.

4.2 Physical conditions and ionic abundances from CELs

Ionic abundances for N^+ , O^+ , O^{+2} , Ne^{+2} , Ar^{+2} , Ar^{+3} , S^+ , S^{+2} , Cl^+ , Cl^{+2} , Fe^+ and Fe^{+2} , were determined for the ESO VLT UVES and SALT HRS data, from the observed CELs using the task *getIonAbundance* from PyNEB. For this we employed the dereddened line intensities listed in Table 3.1 as measured for each data set, and the adopted physical conditions for each nebular zone as presented in Table 3. Since the temperatures derived from [N II], [O III] and [Ar III] line ratios are similar, only one electron temperature was used for the whole nebula, which is the mean value between the temperatures mentioned (the [Ar III] temperature is only available for SALT data). We have verified that this adoption for the temperature value produces equal ionic abundances by using the nebular and auroral lines of the ions. For the density, from data from ESO UVES only a single zone given by [S II] density was assumed, while for SALT data the [S II] density value was used for the low-ionization zone and the [Cl III] density for the more ionized zone. Density values from [Ar IV] and [Fe III] were not considered due to their large uncertainty.

Table 1. Log of ESO-VLT-U2-UVES and SALT HRS observations of Hen 3-1357

Spectrum	Obs. date	Wavelength range (Å)	Spectral res.	Slit width (")	Exp.time (s)	Air mass	Seeing (")
ESO-VLT-U2-UVES							
ADP.2020-06-26T08-14-43.698	2009-03-16	3730-5000	40,970	1.0	600	1.363	1.74
ADP.2020-06-26T08-14-43.724	2009-03-16	5650-9450	42,310	1.0	600	"	1.74
SALT-HRS							
mbgphH202105240022	2021-05-24	3826 - 5583	65,000	1.2	1200	1.170	1.8
mbgphR202105240022	2021-05-24	5473 - 8796	"	"	"	"	1.8
mbgphH202105250025	2021-05-26	3826 - 5583	"	"	600	1.203	1.7
mbgphR202105250025	2021-05-26	5473 - 8796	"	"	"	"	1.7
mbgphH202106240100	2021-06-24	3826 - 5583	"	"	600	1.103	1.7
mbgphH202106240100	2021-06-24	5473 - 8796	"	"	"	"	1.7

**Figure 3.** The diagnostic diagrams for ESO VLT-UVES and SALT HRS data, constructed by using PyNEB, are presented. The diagnostic lines ratios are plotted as a function of the electron temperature and density. They are represented as broken or dotted lines inside a colour band showing the 1σ rms error.

Ionic abundances are given in Table 3. In the same table we included the temperatures, densities, ionic and total abundances presented by the different authors in the period from 1992 to 2021. These data have been taken directly from the publications, without any modification.

In all cases, [O III] electron temperatures are in the range from 10,100 to 11,500 K and [N II] temperatures are in the 10,600 to 12,900 K range, except for the temperatures derived by Otsuka et al. (2017) which are about 2,000 K lower in both cases. The same

occurs for the temperature from [Ar III]. Most probably this is due to Otsuka et al. (2017) used a different set of atomic parameters for both emission-line analyses (CELs and RLs). As they mentioned, effective recombination coefficients, transition probabilities, and effective collision strengths listed in Otsuka et al. (2010) were used, which are different from the parameters used by other authors.

4.3 Physical conditions and ionic abundances from RLs

In this work electron density from O II recombination lines can be derived from the ratio $\lambda\lambda 4649/4661$. The derived values are similar to the values from CELs in both, ESO VLT UVES and SALT HRS observations, however both values present very high uncertainties and thus the density from CELs was adopted for the RLs abundance calculations.

Temperatures from RLs can be derived from He I and O II lines. We followed the methodology from Zhang et al. (2005) for He I temperature using the line ratio $\lambda\lambda 7281/6678$. Equation 1 by Zhang et al. (2005) and the coefficients a_i , b_i and c_i for these lines determined by Benjamin et al. (1999), for a $n_e = 10^4 \text{ cm}^{-3}$, which is adequate to the adopted density for ORLs, were used. To derive temperature from O II lines we followed the methodology proposed by Peimbert et al. (2014), which requires the intensities of O II V1 multiplet and of [O III] $\lambda\lambda 4959, 5007$ lines. The derived values with their uncertainties are listed in Table 3. As expected it is found that both temperatures are lower than the temperatures derived from CELs.

$T_e(\text{He I})$ was used to determine ionic abundances of He⁺ while $T_e(\text{O II})$ was used for all other RLs ionic abundances. Such abundances were computed using PyNEB routine *get.IonAbundance* by using the temperatures and densities mentioned above. The computed values for He⁺, O⁺, C⁺ and N⁺ abundances are listed in Table 3 where the emission lines used for these calculations are marked. The comparison of O⁺ abundances derived from CELs and from RLs allows the determination of the Abundance Discrepancy Factor, ADF, defined as the ratio between the abundance from RLs and the abundance from CELs. The ADFs(O⁺) derived from our data are 3.47 for the ESO VLT UVES data and 2.52 for the SALT data and they are presented in Table 3.

4.4 The temporal behaviour of ionic abundances derived from CELs

By analysing the temporal evolution of ionic abundances presented in Table 3 interesting systematic behaviours are found. In this table it is noticed that O⁺/H⁺ ratio has been decreasing from a value larger than 2.0×10^{-4} in 1992 to 1.44×10^{-4} in 2021. The same happens

Table 2. Line intensities in different epochs, as presented by the different authors^{a,b}

		Parthasarathy et al. (1993)	Arkhipova et al. (2013)	Otsuka et al. (2017)	ESO UVES this work	Arkhipova et al. (2013)	SALT HRS this work
	c(H β)	0.26	0.19	0.08	0.15	0.35	0.22
ion	λ_0	obs 1990	obs 1992	obs 2006	obs 2009	obs 2011	obs 2021
[O II]	3727.00	81.20	58.10	138.86	—	163.00	—
H11	3770.63	—	—	4.35	4.86(0.30)	—	—
H10	3797.90	4.20	4.70	5.33	6.13(0.30)	—	—
He I	3819.60	—	—	1.14	1.40(0.20)	—	—
He I	3833.35	—	—	0.07	0.07(0.02)	—	—
H9	3835.38	6.00	6.40	7.59	7.94(0.40)	—	6.00(1.20)
He I	3867.47	—	—	0.15	0.18(0.07)	—	0.08(0.04)
[Ne III]	3869.06	49.00	—	40.30	51.40(1.02)	—	17.01(1.00)
He I	3871.79	—	—	0.08	0.09(0.01)	—	—
H8	3889.05	17.20+	18.9+	16.00	20.36(1.00)	9.20	20.62(1.20)
He I	3926.54	—	—	0.12	0.13(0.02)	—	0.18(0.10)
He I	3964.73	—	—	0.54	0.94(0.05)	—	0.90(0.09)
[Ne III]	3967.79	—	—	10.00	15.45(0.90)	—	8.85(0.08)
H7	3970.07	32.30+	40.1+	16.03	16.23(0.90)	—	15.71(0.07)
He I	4009.26	—	—	0.15	0.20(0.05)	—	—
He I	4026.20	1.90	2.10	1.53	2.38(0.05)	—	2.42(0.12)
[S II]	4068.60	3.20	3.50	4.47	6.43(0.90)	—	4.93(0.25)
O II	4069.62	—	—	0.27	0.08(0.06)	—	1.67(0.30)
O II	4069.88	—	—	0.38	0.06(0.04)	—	—
O II	4075.86	—	—	0.76	0.09(0.05)	—	—
[S II]	4076.35	0.60	0.60	1.51	2.28(0.44)	—	—
N III	4097.35	—	—	0.02	0.03(0.02)	—	—
H δ	4101.73	24.50	26.70	21.52	25.55(0.90)	21.60	26.11(0.50)
O II	4119.22	—	—	0.02	0.02(0.01)	—	—
He I	4120.81	—	—	0.18	0.23(0.03)	—	—
He I	4143.76	—	—	0.23	0.34(0.03)	—	0.14
O II	4153.30	—	—	0.03	0.03(0.01)	—	—
C II	4267.18	0.07	0.10	0.10	0.12(0.05)	—	0.08(0.04)
H γ	4340.46	43.20	45.70	46.05	46.67(1.00)	50.90	47.34(0.50)
O II	4349.43	—	—	0.03	0.05(0.02)	—	0.09(0.06)
[O III]	4363.21	7.50	7.90	2.46	3.26(0.25)	4.60	2.73(0.35)
He I	4387.93	—	—	0.44	0.65(0.07)	—	0.70(0.40)
He I	4437.55	—	—	0.07	0.08(0.04)	—	—
He I	4471.47	—	5.50	4.63	5.23(0.40)	—	5.55(0.50)
N II	4630.54	—	—	0.02	0.02(0.01)	—	—
O II	4638.86	—	—	0.03	0.04(0.02)	—	0.04(0.03)
O II	4641.81	—	—	0.06	0.08(0.04)	—	0.12(0.02)
O II	4649.13	—	—	0.10	0.13(0.07)	—	0.12(0.02)
O II	4650.84	—	—	0.03	0.03(0.02)	—	—
[Fe III]	4658.05	—	—	0.11	0.17(0.08)	—	0.29(0.03)
O II	4661.63	—	—	0.05	0.04(0.02)	—	0.04(0.02)
O II	4676.23	—	—	0.03	0.03(0.02)	—	0.05(0.03)
[Fe III]	4701.53	—	—	0.05	0.06(0.03)	—	0.10(0.05)
[Ar IV]	4711.37	—	—	0.03	0.04(0.01)	—	< 0.01
He I	4713.22	0.90	1.00	0.67	0.79(0.08)	—	0.85(0.09)
[Fe III]	4733.91	—	—	0.03	0.02(0.01)	—	—
[Ar IV]	4740.16	—	—	0.07	0.06(0.03)	—	< 0.01
[Fe III]	4754.69	—	—	0.03	0.03(0.01)	—	0.06
H β	4861.33	100.00	100.00	100.00	100.00(1.00)	100.00	100.00(1.00)
[Fe III]	4881.00	—	—	0.05	0.08(0.02)	—	0.15(0.07)
He I	4921.93	—	—	1.21	1.45(0.15)	—	1.45(0.12)
[O III]	4931.23	—	—	0.06	0.06(0.03)	—	0.10(0.05)
[O III]	4958.91	305.00	278.50	145.40	138.59(1.00)	148.00	129.65(1.30)
[O III]	5007.06	933.00	860.30	sat	oor	443.90	411.91(2.00)
[Ar III]	5191.82	0.60	—	0.06	oor	—	0.09(0.04)
[Cl III]	5517.72	0.30	0.30	0.12	oor	—	0.10(0.03)
[Cl III]	5537.89	0.40	0.40	0.24	oor	—	0.22(0.02)

^a In the Table, 'sat' indicates saturated line, 'oor': out of range, not observed.^b A '+' indicates blend of two lines.

Table 2 – continued

		Parthasarathy et al. (1993)	Arkhipova et al. (2013)	Otsuka et al. (2017)	ESO UVES this work	Arkhipova et al. (2013)	SALT HRS this work
ion	λ_0	obs 1990	obs 1992	obs 2006	obs 2009	obs 2011	obs 2021
[N II]	5754.64	1.80	2.40	2.58	3.15(0.15)	3.30	2.72(0.12)
He I	5875.60	15.80	15.60	14.67	13.34(0.90)	15.20	11.58(0.55)
[O I]	6300.30	4.10	7.40	16.13	14.59(0.90)	17.70	12.28(0.55)
[S III]	6312.10	1.40	1.70	1.03	1.28(0.15)	1.20	1.14(0.08)
[O I]	6363.78	2.00	2.40	5.10	5.46(0.30)	6.50	4.18(0.12)
[N II]	6527.24	—	—	0.02	0.03(0.02)	—	—
[N II]	6548.04	23.20	20.00	40.96	38.52(1.00)	46.50	42.39(0.84)
H α	6562.82	305.00	286.20	sat	sat	285.50	286.75(2.50)
C II	6578.05	—	—	0.05	0.06(0.03)	—	0.07(0.05)
[N II]	6583.46	78.60	64.90	121.45	sat	144.60	135.22(2.60)
He I	6678.15	4.40	3.80	3.97	4.54(0.30)	4.20	3.74(0.25)
[S II]	6716.44	1.50	1.70	6.07	6.32(0.40)	8.50	5.49(0.20)
[S II]	6730.81	3.00	3.40	12.47	12.20(0.90)	16.10	10.56(0.30)
O I	7002.12	—	—	0.05	0.05(0.02)	—	0.06(0.04)
He I	7062.28	—	—	0.02	0.02(0.01)	0.00	0.02(0.02)
He I	7065.18	9.00	8.50	7.85	8.46(0.40)	7.40	6.27(0.10)
[Ar III]	7135.78	18.50	15.40	10.77	13.95(0.80)	12.30	14.60(0.70)
[Fe II]	7155.16	—	—	0.03	0.05(0.02)	—	0.05(0.01)
[He I]	7160.61	—	—	0.03	0.03(0.01)	—	0.04(0.01)
He I	7281.35	—	0.80	0.73	0.93(0.05)	—	1.19(0.60)
[O II]	7318.92	—	—	4.00	5.61(0.30)	—	6.29(0.40)
[O II]	7319.99	21.8+	18.0+	13.49	17.73(1.00)	—	18.99(0.70)
[O II]	7329.66	—	—	7.48	10.34(1.00)	—	10.64(0.70)
[O II]	7330.73	17.4+	14.3+	6.99	9.76(1.30)	—	9.36(0.40)
[Ni II]	7377.83	—	—	0.03	0.03(0.01)	—	0.03(0.01)
He I	7499.85	—	—	0.04	0.04(0.01)	—	0.04(0.01)
[Ar III]	7751.10	—	3.60	2.63	—	—	2.99(0.15)

with ionic abundances of other highly ionized species like Ne⁺², Ar⁺³, and Ar⁺². On the other hand, the relative abundance of low-ionized species such as O⁺, S⁺, N⁺, and Fe⁺² are increasing with time. All this indicates that the highly-ionized species are recombining in response to the fact that the central star has been cooling down with time.

The fast nebular recombination of highly ionized species is a direct consequence of the high electron density and the fast evolution of the central star. It is known that for a nebula of about 6,000 cm⁻³ the recombination time of H⁺ is less than 20 yr once the ionizing photons flux is closed, and the recombination time of O⁺² is faster due to the larger recombination coefficient (see e.g., [Osterbrock & Ferland 2006](#), Appendix 5, Table A5). The electron density appears to be larger in some zones of Hen 3-1357, therefore a fast recombination of the highly ionized species is expected as the star cools down.

5 DERIVED TOTAL ABUNDANCES. COMPARISON WITH PREVIOUS DETERMINATIONS

Total abundances were determined from the ionic abundances and using some Ionization Correction Factors (ICFs) commonly used in the literature, to correct for the unseen ions. The references for the ICFs employed, their expressions and used values are presented in Appendix A. In Table 3 we present the abundances derived from our data indicating the ICFs used. Also the abundances derived by the different authors are included. Abundances are not expected to vary with time, therefore values derived by the different authors should be similar.

- The values determined for helium abundance between 1990 and 2011 in the different papers are $12 + \log(\text{He}/\text{H}) = 10.97 - 10.98$. Thus the He/H ratio in Hen 3-1357 appears 0.05 dex higher than solar (a value of 10.93 was determined by [Asplund et al. 2009](#)), and slightly lower than the average value found in non-Type I PNe ([Kingsburgh & Barlow 1994](#))³. This value decreases in the observations of SALT 2021 ($12 + \log(\text{He}/\text{H}) = 10.80$), because He⁺ is recombining into He⁰ which is not considered when determining the total He abundance.

- The derived $12 + \log(\text{O}/\text{H})$ values are in the range from 8.4 to 8.6. Therefore the O abundance appears slightly sub solar (solar $12 + \log(\text{O}/\text{H})$ is 8.69 according to [Asplund et al. 2009](#)). The value presented by [Otsuka et al. \(2017\)](#) is slightly larger than the other values due to the lower electron temperatures derived by these authors which induce very large values for O⁺/H⁺, N⁺/H⁺, S⁺/H⁺ and other ions. A similar fact occurs with the SALT-HRS data, where also a low temperature is found, although with very large errors.

- Regarding nitrogen, $12 + \log(\text{N}/\text{H})$ is around 7.7 in all cases (except in [Otsuka et al. 2017](#) where is larger) which is a sub solar value (the solar value is 7.83 as derived by [Asplund et al. 2009](#)).

- Most $12 + \log(\text{S}/\text{H})$ values are around 6.5, a sub solar value ([Asplund et al. 2009](#), reported 7.12).

- $12 + \log(\text{Ne}/\text{H})$ shows values around 7.95, which is very similar to the solar abundance (a value of 7.93 is given by [Asplund et al. 2009](#)).

³ Non-Type I PNe are those belonging to the galactic disc, with N/O abundance ratio ≤ 0.5 by number. The definition of PN Types was proposed by [Peimbert \(1978\)](#)

Table 3. Physical conditions, ionic and total abundances

Authors Obs. year	Partha. 1993 1990	Arkipova 1992	Otsuka 2006	ESO-UVES 2009	Arkipova 2011	SALT HRS 2021
T_e ([N II])	11,000(250)	12,938(2,444)	9,280(100)	12,200 ⁺⁶⁰⁰ ₋₈₀₀	11,066(1752)	10,200 ⁺⁴⁰⁰ ₋₆₀₀
T_e ([O III])	11,000(250)	11,051(755)	9,420(40)	10,500 ⁺²⁰⁰ ₋₃₀₀	11,553(1579)	9,900 \pm 400
T_e ([Ar III])	—	—	8,670(150)	—	—	9,600 ^{+1,300} _{-1,400}
T_e (mean)	—	—	—	11,300 ⁺³⁰⁰ ₋₅₀₀	—	9,900 ⁺⁵⁰⁰ ₋₆₀₀
n_e CELs						
n_e ([S II])	10,000	15,796(10,398)	5,710(1790)	6,800 ⁺⁶⁵⁰⁰ ₋₂₈₀₀	8,740(7701)	6,500 ^{+2,600} _{-1,700}
n_e ([Cl III])	—	7416(5865)	23,970(3120)	—	—	13,600 ^{+18,800} _{-6,400}
n_e ([Ar IV])	—	—	22 720(4360)	31,400 ^{+102,900} _{-23,300}	—	—
n_e ([Fe III])	—	—	—	13,900 ^{+65,800} _{-11,200}	—	23,300 ^{+153,500} _{-17,700}
T_e RLs						
He I- $\lambda\lambda$ 7281/6678	—	—	8340(330)	7,800 \pm 800	—	13,000 ^{+8,400} _{-6,900}
O II-P14	—	—	—	8,100 ⁺⁵⁰⁰ ₋₄₀₀	—	7,900 \pm 300
n_e RLs						
O II- $\lambda\lambda$ 649/61 ^a	—	—	—	10,700:	—	11,000:
X^{+i}/H^{+} CELs						
N ⁺ ($\times 10^{-5}$)	1.30	0.759	3.60	1.81 ^{+0.34} _{-0.17}	2.31	2.82 ^{+0.58} _{-0.34}
O ⁺ ($\times 10^{-5}$)	5.00	2.46	27.00	14.84 ^{+1.87} _{-1.65}	9.10	33.49 ^{+16.01} _{-8.89}
O ²⁺ ($\times 10^{-4}$)	2.44	2.23	1.87	0.96 ^{+0.14} _{-0.08}	1.01	1.44 ^{+0.42} _{-0.23}
Ne ²⁺ ($\times 10^{-5}$)	8.80	5.70	8.41	3.45 ^{+0.61} _{-0.38}	2.09	2.68 ^{+0.77} _{-0.47}
Ar ²⁺ ($\times 10^{-6}$)	—	1.44	1.59	0.96 ^{+0.10} _{-0.08}	0.914	1.24 ^{+0.14} _{-0.10}
Ar ³⁺ ($\times 10^{-8}$)	—	—	2.10	0.95 ^{+0.97} _{-0.94}	—	—
S ⁺ ($\times 10^{-7}$)	2.20	2.96	10.69	8.23 ^{+5.52} _{-2.27}	9.34	9.82 ^{+3.23} _{-1.89}
S ²⁺ ($\times 10^{-6}$)	2.03	2.45	6.82	1.66 ^{+0.35} _{-0.23}	1.43	2.53 ^{+0.22} _{-0.49}
Cl ⁺ ($\times 10^{-8}$)	—	—	1.76	—	—	1.66 ^{+0.30} _{-0.22}
Cl ²⁺ ($\times 10^{-8}$)	—	3.16	10.3	—	—	2.80 ^{+1.0} _{-0.53}
Fe ⁺ ($\times 10^{-8}$)	—	—	—	3.57 ^{+1.61} _{-1.32}	—	79.23 ^{+11.69} _{-8.52}
Fe ²⁺ ($\times 10^{-8}$)	—	—	7.26	4.77 ^{+1.72} _{-2.24}	—	12.98 ^{+3.68} _{-2.55}
X^{+i}/H^{+} RLs						
He ⁺	0.103	—	0.0969	0.089 \pm 0.006	—	0.062 \pm 0.016
O ²⁺ -v1 ($\times 10^{-4}$)	—	—	2.82	3.38 \pm 0.80	—	3.61 ^{+0.57} _{-0.48}
C ²⁺ - λ 4267 ($\times 10^{-5}$)	—	6.91	9.72	10.58 ^{+4.80} _{-4.58}	—	7.40 ^{+3.87} _{-3.98}
N ²⁺ - λ 4631 ($\times 10^{-5}$)	—	—	6.97	9.85 ^{+4.62} _{-5.33}	—	—
ADF(O ²⁺)	—	—	1.51(0.36)	3.47 ^{+0.84} _{-0.89}	—	2.52 ^{+0.60} _{-0.65}
12+log(X/H)						
He/H	11.01	10.97	10.99	10.95 \pm 0.03	10.98	10.80 ^{+0.08} _{-0.13}
O/H	8.48	8.39(0.10)	8.66	8.39 \pm 0.04	8.28(0.19)	8.68 ^{+0.13} _{-0.11}
N/H-KB94	7.81	7.81(0.18)	8.05	7.47 ^{+0.10} _{-0.06}	7.76(0.17)	7.60 ^{+0.08} _{-0.04}
Ne/H-KB94	7.96	7.76(0.11)	8.19	7.95 \pm 0.05	7.54(0.22)	7.95 ^{+0.15} _{-0.13}
Ar/H-KB94	—	6.25(0.11)	6.37	6.25 \pm 0.04	6.00(0.18)	6.36 \pm 0.05
S/H-KB94	6.34	6.78(0.14)	6.83	6.41 ^{+0.13} _{-0.08}	6.38(0.23)	6.55 ^{+0.11} _{-0.08}
Cl/H-DI14	—	4.73(0.11)	5.08	—	—	4.81 ^{+0.08} _{-0.07}
Fe/H-RR05	—	—	5.22	5.15 ^{+0.14} _{-0.16}	—	6.12 \pm 0.05
C/H	—	7.88	8.16	—	—	—
ICFs used	PTP	KB94	DI14	KB94	KB94	KB94
log(N/O)-KB94	-0.67	-0.58	-0.61	-0.90 \pm 0.07	-0.52	-1.08 ^{+0.09} _{-0.08}
log(Ne/O)-KB94	-0.52	-0.64	-0.47	-0.45 \pm 0.02	-0.74	-0.73 \pm 0.02
log(Ar/O)-KB94	—	—	-2.29	-2.13 \pm 0.04	—	-2.32 ^{+0.09} _{-0.11}
log(S/O)-KB94	-2.14	-1.62	-1.83	-1.97 ^{+0.10} _{-0.07}	-1.90	-2.14 \pm 0.07
log(Cl/O)-DI14	—	-3.67	-3.58	—	—	-3.87 \pm 0.09
log(Fe/O)-RR05	—	—	-3.44	-3.24 ^{+0.13} _{-0.17}	—	-2.56 \pm 0.09
log(C/O)	0.18	-0.51	-0.50	—	—	—

^a "—" represents a very uncertain result.

A larger value of 8.19 is found in [Otsuka et al. \(2017\)](#). Possible Ne is enhanced by the production of ^{22}Ne during stellar nucleosynthesis.

- $12+\log(\text{Ar}/\text{H})$ values derived by us are around 6.2, which is a sub solar value ([Asplund et al. 2009](#), reported 6.40 for the Sun).

- $12+\log(\text{Cl}/\text{H})$ values are between 4.7 and 4.8. A higher value of 5.08 is reported in [Otsuka et al. \(2017\)](#). In any case, Cl/H abundance appears highly sub solar, compared with the value of 5.50 reported by [Asplund et al. \(2009\)](#).

- In the case of Fe, the derived values of $12+\log(\text{Fe}/\text{H})$ go from 5.2 to 6.1 and are largely sub solar, more than a hundred times lower than the solar value that according to [Asplund et al. \(2009\)](#) is 7.50. There seems to be a large amount of dust in this nebula. [Otsuka et al. \(2017\)](#) claimed that the largely depleted Fe/H ratio suggests that over 99% of the Fe atoms in the nebula would be locked within silicate grains.

6 DISCUSSION

The N, Ne, Ar and Cl abundances, relative to O, presented in Table 3 show that the Stingray nebula seems to be a normal non-Type I planetary nebula with sub solar abundances.

Nebular abundances can be compared to the predictions of stellar nucleosynthesis models for low-intermediate mass stars at the end of the AGB phase, computed for different masses and different metallicities, to estimate the initial mass of the progenitor star. For instance models by [Karakas \(2010\)](#) and [Ventura et al. \(2017\)](#) (the latter include dust formation) are suitable for this purpose. We found that the chemical abundances of Hen 3-1357 are in agreement with the abundances in [Ventura et al. \(2017\)](#) models with metallicity $Z=0.008$. Such models have initially $\text{He}/\text{H} = 10.95$, $\text{C}/\text{H} = 8.05$, $\text{N}/\text{H} = 7.806$, $\text{O}/\text{H} = 8.56$ and $\text{Ne}/\text{H} = 7.806$, in units of $12+\log(\text{X}/\text{H})$, and evolve towards larger amounts of C and N for masses increasing from 1 to 8 M_{\odot} (see Fig. 1 by [Ventura et al. 2017](#)). Considering the N/H and O/H abundances ratios in Hen 3-1357, we can conclude that the star SAO 244567 had an initial mass between 1.0 to 1.5 M_{\odot} because the nebular N is not enhanced as it should be for stars with initial masses equal or larger than 2 M_{\odot} . A similar result was obtained by [Otsuka et al. \(2017\)](#) analysing [Karakas \(2010\)](#) models.

However the fast variations of the central star, which in about 20 years evolved from a post-AGB B1 supergiant to a young planetary nebula central star with an effective temperature of about 60,000 K around 2002, and afterwards started cooling down up to 41,000 K in 2011 ([Arkhipova et al. 2013](#)) do not correspond to the normal evolution of such a single low-mass star in advanced stage of evolution.

The subsequent fall in the nebular excitation degree, which we have demonstrated in this work, shows that the stellar temperature is still decreasing. By using the procedure described by [Arkhipova et al. \(2013\)](#) based on an empirical relation determined by [Kaler \(1978\)](#), which uses the $[\text{O III}]5007/\text{H}\beta$ line ratio, we estimated the present effective temperature of the central star to be less than about 40,000 K which confirms that SAO 244567 is still cooling down.

A Late Thermal Pulse (LTP) has been suggested to explain these changes. If such a hypothesis is confirmed, the star should continue cooling down all the way towards the AGB phase.

Following the fast evolution of the central star, the nebula has shown rapid changes. The ionization degree of its heavy elements, which increased fast in the 1970 to 1990 period is now decreasing and there is much evidence that such elements are presently recombining.

7 CONCLUSIONS

From high resolution spectra obtained in 2009 with the ESO VLT UVES spectrograph, and in 2021 with the SALT HRS spectrograph, physical conditions and chemical abundances have been obtained for the extraordinary and fast evolving planetary nebula Hen 3-1357, the Stingray Nebula. Our line intensities, physical conditions and chemistry have been compared with values from the literature, derived from 1990 to 2021. We have confirmed that the nebula is presently recombining as a result of the fast cooling of the central star whose effective temperature has decreased from about 60,000 K in 2002 to less than 40,000 K in 2021.

The chemical abundances have been derived from CELs for a number of elements. Also chemical abundances have been derived from RLs and the derived $\text{ADF}(\text{O}^{+2})$ has a value of 3.5 from ESO VLT UVES data and 2.6 from SALT HRS data. This value for the $\text{ADF}(\text{O}^{+2})$ is within the usual values derived for PNe (see [McNabb et al. 2013](#) for a compilation of ADF values in a large sample of PNe). A slightly lower $\text{ADF}(\text{O}^{+2})$ value of 1.51 was derived by [Otsuka et al. \(2017\)](#) for Hen 3-1357.

Our abundance values are in general agreement with values from the literature, and show that Hen 3-1357 have sub solar O, N, S, and Ar abundances, corresponding to a central star of initial mass similar or lower than 1.5 M_{\odot} .

The fast evolution of the central star of such a mass is unexpected and it has important consequences in the nebular behaviour which is fast recombining. If the central star experienced a LTP, as claimed by [Reindl et al. \(2014, 2017\)](#) and [Lawlor \(2021\)](#), it should keep cooling down in its way towards the AGB phase. Both, star and nebula, require a close follow up in order to get deeper insight of this phenomenon and to improve our understanding of the low-mass stellar evolution.

ACKNOWLEDGEMENTS

Some of the observations reported in this paper were obtained with the Southern African Large Telescope (SALT). We are thankful to Prof. Patricia Whitelock for her help in getting the SALT time. F. Ruiz-Escobedo acknowledge scholarship from CONACyT-México. M. Parthasarathy is thankful to Prof. Keivan Stassun, and dean, chairman and faculty of the department of Physics and Astronomy, Vanderbilt University, for their kind hospitality and support. This work received financial support from PAPIIT-UNAM grant IN105020.

DATA AVAILABILITY

The data underlying this article will be shared on reasonable request to the corresponding author.

REFERENCES

- Arkhipova, V. P., Ikonnikova N. P., Kniazev, A. Y., Rajoelimanana, A., 2013, *AstL*, 39, 201
- Asplund, M., Grevesse, N., Sauval, A. J., Scott, P., 2009, *ARA&A*, 47, 481
- Bautista, M. A., Fivet, V., Ballance, C., et al. *ApJ*, 808, 174
- Balick, B., Guerrero, M. A., Ramos Larios, G., *ApJ*, 907, 104
- Benjamin R. A., Skillman E.D., Smits D.P., 1999, *ApJ*, 514, 307
- Bobrowsky, M., Sahu, K. C., Parthasarathy, M., García-Lario, P., 1998, *Nature*, 392, 469
- Butler K., Zeippen C. J., 1989, *A&A*, 208, 337
- Cardelli, J. A. A., Clayton, G. C., Mathis, J. S. 1989, *ApJ*, 345, 245
- Delgado-Inglada, G., Morisset, C., Stasinska, G., 2014, *MNRAS*, 440, 536

Dopita, M. A. & Meatheringham, S. J., 1990, *ApJ*, 357, 140.
 Fang X., Storey P.J., Liu X.-W., 2011, *A&A*, 530, A18
 Feibelman, W. A. 1995, *ApJ*, 443, 245
 Frew, D. J., Parker, Q. A., Bojicic, I. S., 2016, *MNRAS*, 455, 1459
 Froese Fischer C., Tachiev G., 2004, *At. Data Nucl. Data Tables*, 87, 1
 Galavís M.E., Mendoza C., Zeippen C.J., 1995, *A&AS*, 111, 347
 Galavís M.E., Mendoza C., Zeippen C.J., 1997, *A&AS*, 123, 159
 Harvey-Smith, L., Hardwick, J. A., de Marco, O., Parthasarathy, M., Gonidakis, I., Akhter, S., Cunningham, M., 2018, *MNRAS*, 479, 1842
 Henize, K. G., 1967, *ApJS*, 14, 125
 Henize, K. G., 1976, *ApJS*, 30, 491
 Johansson, S., Zethson, T., Hartman, H., Ekberg, J. O. et al., 2000, *A&A*, 361, 977
 Kaler, J. B., 1978, *ApJ*, 220, 887
 Karakas, A. I., 2010, *MNRAS*, 403, 1413
 Kaufman V., Sugar J., 1986, *J. Phys. Chem. Ref. Data*, 15, 343
 Kisielius R., Storey P.J., Ferland G.J., Keenan F.P., 2009, *MNRAS*, 397, 903
 Kingsburgh, R. L., Barlow, M. J., 1994, *MNRAS*, 271, 254
 Kniazev, A., 2016, MIDAS automatic pipeline for HRS data, SALT report HRS0000006
 Kniazev, A., 2017, The list of spectrophotometric standars for HRS, SALT report HRS0000007
 Lawlor, T. M., 2021, *MNRAS*, 504, 667
 Liu X.-W., Storey P. J., Barlow M. J., et al., 2000, *MNRAS*, 312, 585
 Luridiana, V., Morisset, C., Shaw, R. A., 2015, *A&A*, 573, A42
 McNabb, I. A., Fang, X., Liu, X.-W., Bastin, R. J., Storey, P. J., 2013, *MNRAS*, 428, 3443
 Miller-Bertolami, M. M., 2016, *A&A*, 588, 25
 Mendoza C., Zeippen C. J., 1982, *MNRAS*, 198, 127
 Mendoza C., 1983, *IAU Symp.*, 103, 143
 McLaughlin B.M., Bell K.L. 2000, *J. Phys. B*, 33, 597
 Otsuka, M., Tajitsu, A., Hyung, S., Izumiura, H., 2010, *ApJ*, 723, 658
 Otsuka, M., Parthasarathy, M., Tajitsu, A., Hubrig, S. 2017, *ApJ*, 838, 710
 Osterbrock, D., Ferland, G., in *Astrophysics and Gaseous Nebular and Active Galactic Nuclei*, second edition, University Science Books.
 Parthasarathy, M., Pottasch, S. R. 1989, *A&A*, 154, L16
 Parthasarathy, M., Garcia-Lario, P., Pottasch, S. R., et al. 1993, *A&A*, 267L, 19
 Parthasarathy, M., Garcia-Lario, P., de Martino, D., Pottasch, S. R., Kilkenny, D., Martinez, P., Sahu, K. C., Reddy, B. E., Sewell, B. T. 1995, *A&A*, 300, L25
 Pequignot D., Petitjean P., Boisson C., 1991, *A&A*, 251, 680
 Peimbert, M., Planetary Nebulae: Observations and Theory, *IAU Symp. No. 76*, p. 215, ed. Burton, W.B., Reidel, Dordrecht.
 Peimbert A., Peimbert M., Delgado-Inglada G., García-Rojas J., Peña M., 2014, *Rev. Mex. Astron. Astrofis.*, 50, 329
 Podobedova L.I., Kelleher D.E., Wiese, W.L., 2009, *J. Phys. Chem. Ref. Data*, 38, 171
 Porter R.L., Ferland G.J., Storey P.J., Detisch M.J., 2012, *MNRAS*, 425, L28
 Porter R.L., Ferland G.J., Storey P.J., Detisch M. J., 2013, *MNRAS*, 433, L89
 Quinet, P., 1996, *A&AS*, 116, 573
 Reindl, N., Rauch, T., Parthasarathy, M., Werner, K., Kruk, J. W., Hamann, W.-R., Sander, A., Todt, H., 2014, *A&A*, 565, A40
 Reindl, N., Rauch, T., Miller Bertolami, M. M., Todt, H., Werner, K. 2017, *MNRAS*, 464, L51
 Ramsbottom, C. A., Bell, K. L., 1999, *Atomic Data and Nuclear Data Tables*, 66, 1
 Rodríguez M., Rubin R.H., 2005, *ApJ*, 626, 900
 Schaefer, B.E., Edwards, Z., 2015, *ApJ*, 812, 133
 Storey, P. J., Hummer, D. G., 1995, *MNRAS*, 272, 41
 Storey P. J., Zeippen C. J., 2000, *MNRAS*, 312, 813
 Storey P. J., Sochi T., Badnell N.R., 2014, *MNRAS*, 441, 3028
 Storey P. J., Sochi T., Bastin R., 2017, *MNRAS*, 470, 379
 Tayal S. S., Gupta G. P., 1999, *ApJ*, 526, 544
 Tayal S. S., 2004, *A&A*, 418, 363
 Tayal S. S., Zatsarinny O., 2010, *ApJS*, 188, 32
 Tayal S. S., 2011, *ApJS*, 195, 12

Ventura, P., Stanghellini, L., Dell’Agli, F., García-Hernández, D. A., 2017, *MNRAS*, 471, 4648
 Zhang H., 1996, *A&AS*, 119, 523
 Zhang Y., Liu X.-W., Liu Y., Rubin R.H., 2005, *MNRAS*, 358, 457

APPENDIX A: IONIZATION CORRECTION FACTORS

Expressions and ICFs used for the total abundances calculation are listed next.

- $\frac{\text{He}}{\text{H}} = \frac{\text{He}^+}{\text{H}^+}$.
- $\frac{\text{O}}{\text{H}} = \frac{\text{O}^+ + \text{O}^{+2}}{\text{H}^+}$, $\text{ICF}(\text{ESO} - 09) = \text{ICF}(\text{SALT} - 21) = 1.00$.
- $\frac{\text{N}}{\text{H}} = \text{ICF}(\text{N}) \times \frac{\text{N}^+}{\text{H}^+}$. $\text{ICF}(\text{N}) = \frac{\text{O}}{\text{O}^+}$ (Kingsburgh & Barlow 1994). $\text{ICF}(\text{ESO} - 09) = 1.65$, $\text{ICF}(\text{SALT} - 21) = 1.44$.
- $\frac{\text{Ar}}{\text{H}} = \text{ICF}(\text{Ar}) \times \frac{\text{Ar}^{+2} + \text{Ar}^{+3} + \text{Ar}^{+4}}{\text{H}^+}$, $\text{ICF}(\text{Ar}) = \frac{1}{1 - \text{N}^+/\text{N}}$. If only Ar^{+2} is detectable, $\frac{\text{Ar}}{\text{H}} = 1.87 \times \frac{\text{Ar}^{+2}}{\text{H}^+}$ (Kingsburgh & Barlow 1994). $\text{ICF}(\text{ESO} - 09) = 2.54$, $\text{ICF}(\text{SALT} - 21) = 1.87$.
- $\frac{\text{Ne}}{\text{H}} = \text{ICF}(\text{Ne}) \times \frac{\text{Ne}^{+2}}{\text{H}^+}$. $\text{ICF}(\text{Ne}) = \frac{\text{O}}{\text{O}^{+2}}$ (Kingsburgh & Barlow 1994). $\text{ICF}(\text{ESO} - 09) = 2.53$, $\text{ICF}(\text{SALT} - 21) = 2.19$.
- $\frac{\text{S}}{\text{H}} = \text{ICF}(\text{S}) \times \frac{\text{S}^+ + \text{S}^{+2}}{\text{H}^+}$. $\text{ICF}(\text{S}) = \left[1 - \left(1 - \frac{\text{O}^+}{\text{O}} \right)^3 \right]^{-1/3}$ (Kingsburgh & Barlow 1994). $\text{ICF}(\text{ESO} - 09) = 1.02$, $\text{ICF}(\text{SALT} - 21) = 1.01$.
- $\frac{\text{Cl}}{\text{O}} = \text{ICF}(\text{Cl}) \times \frac{\text{Cl}^+ + \text{Cl}^{+2}}{\text{O}^+}$. $\text{ICF}(\text{Cl}) = 1$ (Delgado-Inglada et al. 2014). $\text{ICF}(\text{ESO} - 09) = --$, $\text{ICF}(\text{SALT} - 21) = 1.00$.
- $\frac{\text{Fe}}{\text{O}} = \frac{\text{Fe}^+ + \text{Fe}^{+2}}{\text{O}^+}$, (Rodríguez & Rubin 2005). $\text{ICF}(\text{ESO} - 09) = \text{ICF}(\text{SALT} - 21) = 1.00$.

APPENDIX B: ATOMIC DATA

This paper has been typeset from a \LaTeX file prepared by the author.

Table B1. Atomic parameters used in PyNEB calculations

Ion	Transition probabilities	Collisional strenghts
N ⁺	Froese Fischer & Tachiev (2004)	Tayal (2011)
O ⁺	Froese Fischer & Tachiev (2004)	Kisieliuss et al. (2009)
O ⁺²	Froese Fischer & Tachiev (2004) Storey & Zeippen (2000)	Storey, Sochi, & Badnell (2014)
Ne ⁺²	Galavís et al. (1997)	McLaughlin & Bell (2000)
S ⁺	Podobedova, Kelleher, & Wiese (2009)	Tayal & Zatsarinny (2010)
S ⁺²	Podobedova, Kelleher, & Wiese (2009)	Tayal & Gupta (1999)
Cl ⁺	Mendoza (1983)	Tayal (2004)
Cl ⁺²	Mendoza (1983)	Butler & Zeippen (1989)
Ar ⁺²	Mendoza (1983) Kaufman & Sugar (1986)	Galavís, Mendoza, & Zeippen (1995)
Ar ⁺³	Mendoza & Zeippen (1982) Kaufman & Sugar (1986)	Ramsbottom & Bell (1997)
Fe ⁺	Bautista et al. (2015)	Bautista et al. (2015)
Fe ⁺²	Quinet (1996) Johansson et al. (2000)	Zhang (1996)
Ion	Effective recombination coefficients	
H ⁺	Storey & Hummer (1995)	
He ⁺	Porter et al. (2012, 2013)	
N ⁺²	Fang et al. (2011)	
O ⁺²	Storey, Sochi, & Bastin (2017)	
C ⁺²	Pequignot, Petitjean, & Boisson (1991)	